Phys Chem Minerals (2011) 38:665–678
DOI 10.1007/s00269-011-0439-y

ORIGINAL PAPER

The enigma of post-perovskite anisotropy: deformation versus transformation textures

Lowell Miyagi · Waruntorn Kanitpanyacharoen · Stephen Stackhouse · Burkhard Militzer · Hans-Rudolf Wenk

Received: 31 March 2011 / Accepted: 21 May 2011 / Published online: 5 June 2011

Abstract The D″ region that lies just above the core mantle boundary exhibits complex anisotropy that this is likely due to preferred orientation (texturing) of the constituent minerals. (Mg,Fe)SiO_3 post-perovskite is widely thought to be the major mineral phase of the D″. Texture development has been studied in various post-perovskite phases ($MgSiO_3$, $MgGeO_3$, and $CaIrO_3$), and different results were obtained. To clarify this controversy, we report on transformation and deformation textures in $MgGeO_3$ post-perovskite synthesized and deformed at room temperature in the diamond anvil cell. Transformed from the enstatite phase, $MgGeO_3$ post-perovskite exhibits a transformation texture characterized by (100) planes at high angles to the direction of compression. Upon subsequent deformation, this texture changes and (001) lattice planes become oriented nearly perpendicular to compression, consistent with dominant (001)[100] slip. When $MgGeO_3$ post-perovskite is synthesized from the perovskite phase, a different transformation texture is observed. This texture has (001) planes at high angle to compression and becomes slightly stronger upon compression. We also find that the yield strength of $MgGeO_3$ post-perovskite is dependent on grain size and texture. Finer-grained samples exhibit higher yield strength and are harder to induce plastic deformation. Strong textures also affect the yield strength and can result in higher differential stresses. The inferred dominant (001) slip for pPv is significant for geophysics, because, when applied to geodynamic convection models, it predicts the observed anisotropies of S-waves as well as an anti-correlation between P- and S-waves.

Keywords Post-perovskite · $MgGeO_3$ · Texture · Anisotropy · Deformation · Transformation · D″

L. Miyagi (✉)
Department of Geology and Geophysics,
Yale University, New Haven, CT 06511, USA
e-mail: lowell.miyagi@yale.edu

L. Miyagi · W. Kanitpanyacharoen · B. Militzer · H.-R. Wenk
Department of Earth and Planetary Science,
University of California, Berkeley, CA 94720, USA

S. Stackhouse
School of Earth and the Environment,
University of Leeds, Leeds LS2 9JT, UK

Introduction

The D″ region lies just above the core mantle boundary (CMB). In contrast to the bulk of the lower mantle, this ~200-km-thick layer possesses considerable seismic complexity, characterized by seismic discontinuities, large topographic variations, significant lateral heterogeneity, anisotropy, and ultra-low-velocity zones (ULVZ) (e.g. Helmberger et al. 2005; Lay and Garnero 2007; Garnero and McNamara 2008). Of particular significance is a D″ anisotropy of shear waves in the circum-Pacific (Panning and Romanowicz 2004, 2006; Wookey and Kendall 2007) with $V_{SH} > V_{SV}$, where V_{SH} and V_{SV} are the velocities of shear waves polarized parallel and perpendicular to the core mantle boundary, respectively.

Numerical modeling (McNamara et al. 2002, 2003) and laboratory experiments (Loubet et al. 2009) indicate that deformation is enhanced near boundary layers, and large-strain deformation is expected to occur in the D″ region, particularly in subducted slabs. Experimental (Hunt et al. 2009) and theoretical (Ammann et al. 2010) evidence

suggests that the D″ layer is weaker than the overlying mantle and would be expected to localize deformation. Thus, anisotropy may be due to deformation induced texturing of its constituent minerals.

At conditions closely corresponding to those of the CMB (127 GPa and 2,500 K), $MgSiO_3$ undergoes a solid–solid phase transition from perovskite (Pv) to post-perovskite (pPv) (Murakami et al. 2004; Oganov and Ono 2004; Shim et al. 2004). Many physical properties of pPv, such as the steep Clapeyron slope and predicted seismic velocities, support the presence of pPv, at least in the high-velocity circum-Pacific region of the D″ (Lay and Garnero 2007; Shim 2008).

Although texture is vital to understanding the D″, information on deformation mechanisms for pPv is limited and controversial. Among the mechanisms that produce texture, slip by dislocation glide has received the most attention and was approached based on crystal structure features, first principles modeling, and high pressure experiments. Due to the layered nature of the pPv structure, early studies proposed that slip should occur along the layers, on the (010) plane (Murakami et al. 2004; Oganov and Ono 2004; Iitaka et al. 2004). However, Oganov et al. (2005) predicted slip on $\{110\}\langle 1\bar{1}0\rangle$ based on first-principles metadynamics and energetics of stacking faults. Modeling of dislocation cores based on the Peierls–Nabarro model predicted (010)[001] to be the easy slip system in $MgSiO_3$ pPv (Carrez et al. 2007a, b). Metsue et al. (2009) expanded this work and concluded that the easiest slip system is (010)[001] for $CaIrO_3$ pPv and (001)[100] for $MgGeO_3$ pPv.

On the experimental side, most work has concentrated on the pPv analog $CaIrO_3$ that is stable at ambient pressure. Transmission electron microscopy (TEM) studies identified Burgers vectors $b = [100]$ (Miyajima et al. 2006; Walte et al. 2007; Miyajima and Walte 2009) with minor occurrence of $b = \langle u0w\rangle$ (Miyajima et al. 2006), suggesting slip on (010). Fabric observations using electron back-scatter diffraction (EBSD) on samples recovered from high-temperature shear (Yamazaki et al. 2006; Walte et al. 2007) and coaxial shortening (Walte et al. 2007) experiments also inferred (010)[100] slip in $CaIrO_3$ pPv. Room temperature DAC experiments on $CaIrO_3$ pPv produced textures consistent with (010) slip, showing that the dominant slip plane is the same at room- and high temperatures (Niwa et al. 2007). In situ radial diffraction texture measurements on $CaIrO_3$ pPv deformed in the D-DIA also indicate that texture and dominant slip systems did not change with temperature, pressure, or strain rate, and, based on polycrystal plasticity modeling identified (010)[100] and minor (010)⟨101⟩ slip, showed that (010)[001] slip was incompatible with the experiment (Miyagi et al. 2008a). Thus, the conclusion that slip on (010)[100] is dominant in $CaIrO_3$ is quite robust based on a number of independent studies.

Santillán et al. (2006) performed experiments on the analog Mn_2O_3 pPv and found both (010) and (100) slip. Initially, it appears that (010) lattice planes are oriented perpendicular to compression, but after annealing (100) and {110}, planes were oriented at high angles to compression. It is difficult to assess the implications of this experiment as X-ray diffraction was taken in axial geometry that is not suitable for quantifying texture patterns.

Deformation experiments on the mantle pPv phase $MgSiO_3$ or its close structural analog $MgGeO_3$ are difficult because these phases are only stable at very high pressure and cannot be quenched. In situ texture observations with diamond anvil cells use diamonds not only to produce high hydrostatic pressure but also as pistons to produce compressive stress. In radial diffraction geometry, textures with (100) planes at high angles to compression were observed, both for $MgGeO_3$ pPv (Merkel et al. 2006) and $MgSiO_3$ pPv (Merkel et al. 2007). This is consistent with slip on {110} and/or (100). By contrast, recent DAC experiments on $MgSiO_3$ pPv (Miyagi et al. 2010), with large strain and strong texture development, aligned (001) planes perpendicular to compression, implying (001)[100] slip. Recently, $MnGeO_3$ pPv was deformed at pressures up to $\sim$110 GPa and 2,000 K using a laser-heated DAC, and textures are consistent with (001) slip (Hirose et al. 2010).

It has been suggested that some experiments recorded transformation textures rather than deformation textures (Santillán et al. 2006; Walte et al. 2007, 2009; Miyagi et al. 2010; Okada et al. 2010). In $CaIrO_3$, transformation from Pv to pPv generates a texture of (100) planes nearly normal to the compression directions (Walte et al. 2009), similar to textures observed in $MgGeO_3$ pPv (Merkel et al. 2006) and $MgSiO_3$ pPv (Merkel et al. 2007). However, in DAC experiments on $MgGeO_3$ pPv, after transformation of Pv to pPv, (001) planes were oriented at high angles to compression (Okada et al. 2010).

Differences between textures in $CaIrO_3$, Mn_2O_3, $MnGeO_3$ $MgGeO_3$, and $MgSiO_3$ pPv may be due to different structural features (Miyagi et al. 2008a). In terms of bond lengths, bond angles and octahedral distortions $CaIrO_3$ pPv has very different structural parameters than $MgSiO_3$ pPv and $MgGeO_3$ pPv (Kubo et al. 2008). Raman spectroscopy indicates that bonding in $CaIrO_3$ pPv is different from other pPv-structured compounds (Hustoft et al. 2008a), and first-principles computations find $CaIrO_3$ pPv to have elastic properties and electronic structure inconsistent with $MgSiO_3$ pPv (Tsuchiya and Tsuchiya 2007). Modeling of dislocation cores finds that $CaIrO_3$ is much more plastically anisotropic than $MgSiO_3$ pPv (Metsue et al. 2009).

With this background of uncertainties and seeming contradictions, we undertook this study to explore in more detail issues of deformation versus transformation textures, the influence of the starting material, and the influence of microstructure, especially grain size. As material we chose $MgGeO_3$ that appears to be a close analog to $MgSiO_3$ in the lowermost mantle.

Experimental procedure

Three experiments were performed at beamline 16 ID-B of the HP-CAT sector of the Advanced Photon Source at Argonne National Laboratory, Argonne, IL. A panoramic-type cell was used for Runs 1 and 2, while a gas membrane–driven modified Mao-Bell-type cell with large openings for radial diffraction was used in Run 3. Beveled anvils with an 8° bevel angle, 300 μm outer culet, and a 150 μm inner culet were assembled in the DAC. Beryllium gaskets of Be alloy I-220-H with a 3 mm outer diameter were pre-compressed, then the sample chamber was drilled using electron discharge machining (EDM). For Runs 1 and 2, gaskets were pre-compressed to 30 μm thickness, and a 50-μm-diameter sample chamber was drilled. In Run 3, thickness was 27 μm and the sample chamber was 35 μm. Starting material of finely ground polycrystalline $MgGeO_3$ enstatite was mixed with 10 wt% Pt powder to serve as a laser absorber and online pressure calibrant. No pressure medium was used to maximize deviatoric stress. Diffraction images were collected in radial diffraction geometry where the X-ray beam is orthogonal to the compression axis. To minimize diffraction from the Be gaskets, the samples were tilted 20° about an axis perpendicular to the compression direction in Runs 1 and 2, and 15° in Run 3. Samples were compressed to high pressure and then heated using single-sided laser heating to induce the phase transformation. Pressures were calculated using the equation of state (EOS) for $MgGeO_3$ pPv from Kubo et al. (2006). In Run 1, the sample was converted to pPv at 2,100 K, and after heating, pressure was 81.1 GPa. Conversion temperature for Run 2 was 1,800 K, and pressure measured just after heating was 82.5 GPa. In Run 3, the sample was first converted to the Pv phase at ~35 GPa and 1,600 K and was then further compressed and heated at 2,025 K. After heating, pressure was 75.8 GPa. Once conversion to pPv was achieved, pressure was increased incrementally at room temperature, recording in situ radial X-ray diffraction images on a MAR3450 image plate at each pressure step. During exposures of ~100 s, samples were oscillated ±5° about an axis perpendicular to compression in order to improve grain statistics. X-ray wavelength was 0.412419 Å and beam size was 10 × 10 μm. Sample to detector distance, beam center, instrument broadening, and detector tilt were calibrated using a CeO_2 standard.

Data analysis

Synchrotron diffraction images were first processed with Fit2d (Hammersley 1997). Images were integrated over 5° azimuthal arcs into 72 spectra and "unrolled" (Fig. 1). Spectra containing the beam-stop arm and diamond spots were removed. Diffraction images were analyzed using the Rietveld method as implemented in the software package MAUD (Lutterotti et al. 1997). A Q range of 1.17–4.14 $Å^{-1}$ was used ($Q = 2\pi/d$-spacing). Backgrounds were interpolated using fifteen points, manually selected between diffraction peaks. Images were refined for lattice parameters, crystallite size, lattice strains, and preferred orientation. For the determination of crystallite size, Popa line broadening with an isotropic size-strain model was used (Popa and Balzar 2002). For X-ray diffraction, there are three sources of line broadening, instrument broadening that is corrected with the CeO_2 standard, domain size, and microstrains that refers to heterogeneous local strains. For the correction of instrument broadening, it is assumed that the calibration standard is well enough crystallized that the contribution of finite crystallite size and microstrain is negligible compared to instrument broadening (Lutterotti 2006). In the Rietveld refinement, a convolution of Gauss and Lorentz functions (i.e. Voigt function) is used for the fitting of diffraction peak profiles. Microstrain broadening is associated with the Gaussian coefficient and diffraction order dependent, while size broadening is associated with the Lorentzian component and is diffraction order independent (Popa and Balzar 2002). Elastic strains imposed by the deformation device result in variations in lattice spacing with respect to the compression direction. These are apparent in radial diffraction images as variations in peak positions with azimuth (Fig. 1). Plastic deformation by dislocation glide results in crystal rotations that generate texture. Texture appears as systematic intensity variations along Debye rings (Fig. 1).

The moment pole stress model (Matthies and Humbert 1993; Matthies et al. 2001) was used to refine elastic lattice strains and calculate stresses. A bulk path geometric mean (Matthies et al. 2001), which lies between the Voigt and Reuss bounds, was assumed for the micromechanical model. The moment pole stress model is similar to that of Singh (1993) and Singh et al. (1998) but allows more complicated deformation geometries and accounts for preferred orientation. For axial compression, the stress tensor σ_{ij} can be separated into hydrostatic (σ_p) and differential stress (D_{ij}) components such that

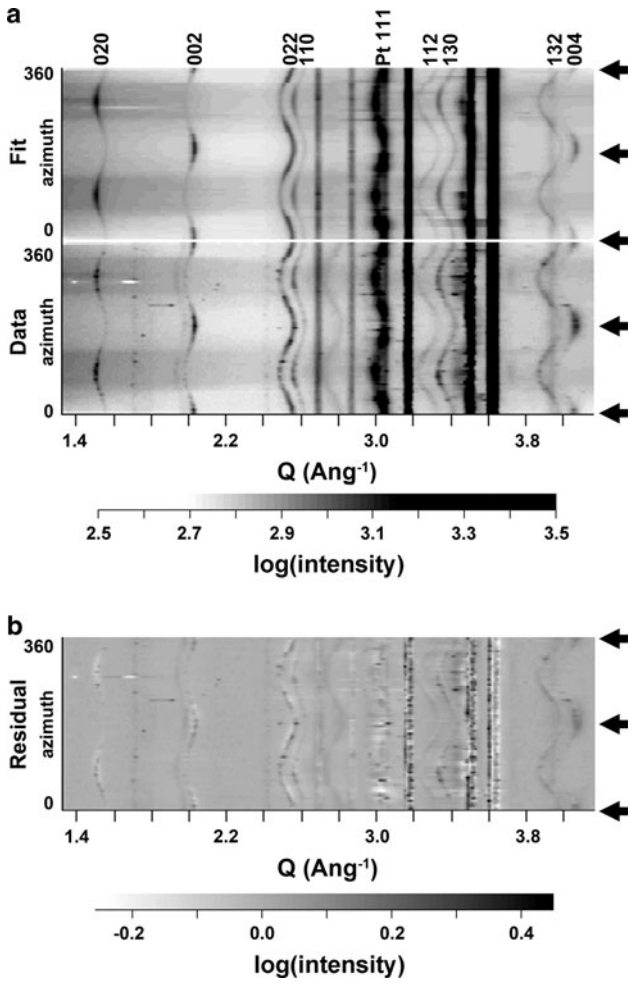

Fig. 1 **a** "Unrolled" diffraction image of $MgGeO_3$ pPv taken in situ at 127 GPa (*bottom*) with the fit from Rietveld refinement (*top*). The residual of the fitting is shown in **b**. Note the excellent correlation between the data and the model fit. pPv diffraction peaks are labeled, and black arrows indicate the compression direction. Straight lines are Be and BeO diffraction peaks from the gasket. The Pt 111 peak is also labeled. Texture is evident as systematic intensity variations along diffraction peaks. Deviatoric stress can be calculated from the variation of peak position with azimuth, which is observed in the diffraction image

$$\sigma ij = \begin{bmatrix} \sigma p & 0 & 0 \\ 0 & \sigma p & 0 \\ 0 & 0 & \sigma p \end{bmatrix} + \begin{bmatrix} -t/3 & 0 & 0 \\ 0 & -t/3 & 0 \\ 0 & 0 & 2t/3 \end{bmatrix} = \sigma p + Dij,$$

where t is the axial stress component and provides a lower bound estimate for the yield strength (Singh 1993, 1998). For these refinements, differential stresses were fixed with $\sigma_{11} = \sigma_{22}$ and $\sigma_{33} = -2\sigma_{11}$, where σ_{33} is the largest principal stress and is negative for compression, according to the conventions in MAUD.

Elastic constants for $MgGeO_3$ pPv are necessary for estimating differential stresses, and we chose to calculate the elastic tensor theoretically. Calculations based on density functional theory (Hohenberg and Kohn 1964; Kohn and Sham 1965) and projector-augmented wave method (Blöchl 1994; Kresse and Joubert 1999) were performed using the VASP code (Kresse and Furthmüller 1996a, b), with elastic constants determined for a temperature of 0 K from stress–strain relations using the finite-difference approach (Karki et al. 2001). Three orthorhombic and one triclinic strains of magnitude ±0.5% were used. The exchange–correlation functional used adhered to the Perdew–Burke–Ernzerhof form of the generalized gradient approximation (Perdew et al. 1996). The kinetic energy cutoff for the plane-wave expansion was 1,000 eV, and the Brillouin zone was sampled using a 10 × 6 × 6 k-point grid (Monkhorst and Pack 1976). This ensured that the elastic constants converged to within less than one percent. Since the generalized gradient approximation overestimates pressure, a correction was estimated from the experimental data of Kubo et al. (2008), using the method of Oganov et al. (2001). When determining the correction, the thermal pressure term was neglected, but it is expected to be less than 1 GPa at room temperature (Karki 2000). The −15 GPa correction shifts the equation of state to lower pressure, in better agreement with experimental results. Our elastic constants are shown in Fig. 2 and are given in Table 1. Excellent agreement is found with the results of Usui et al. 2010 who computed the elastic constants between 0 and 100 GPa, also with calculations based on density functional theory, but using perturbation theory.

The tomographic E-WIMV algorithm was used to calculate the orientation distribution (OD). This is similar to the WIMV model of Matthies and Vinel (1982) but allows incomplete and arbitrary pole figure coverage. Textures are first refined without imposing symmetry to verify approximate axial symmetry about compression (Ischia et al. 2005; Speziale et al. 2006). Cylindrical symmetry is then imposed about the compression axis, consistent with the geometry of axial compression. Axial compression textures can be compactly represented by an inverse pole figure (IPF), showing the relationship between crystallographic directions of crystallites to the compression direction. $MgGeO_3$ pPv has orthorhombic crystal symmetry (Cmcm); thus, only one quadrant of the inverse pole figure is needed to represent the OD. Pole densities are given in multiples of random distribution (m.r.d.), where m.r.d. = 1 corresponds to a random distribution and an m.r.d. of infinity corresponds to a single crystal texture.

Results

Table 2 shows Rietveld refinement results for lattice parameters (unit cell parameters corrected for non-hydrostatic stresses), crystallite size, axial stress component t,

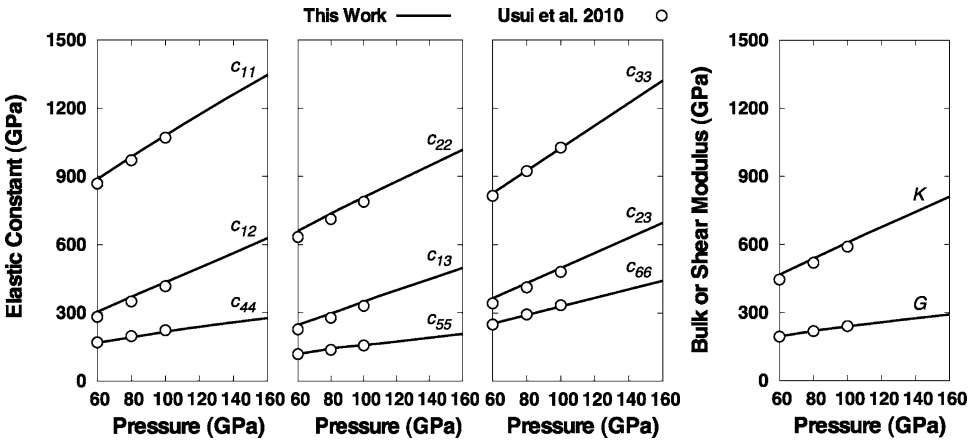

Fig. 2 Calculated isothermal elastic constants, bulk elastic moduli, and their pressure dependence for $MgGeO_3$ pPv. Excellent agreement is found with the values of Usui et al. (2010). Elastic constants are used for the calculation of differential stresses. Note that C_{22} is softer than C_{11} or C_{33}, indicating high compressibility of the pPv structure perpendicular to the layering on (010), consistent with a layered structure. Additionally, C_{66} is stronger than C_{44} or C_{55}, which paradoxically indicates resistance to shearing along the (010) layering. This is similar to $MgSiO_3$ pPv (Stackhouse et al. 2005; Wentzcovitch et al. 2006; Stackhouse and Brodholt 2007)

Table 1 Calculated values for pressure, corrected pressure, unit cell parameters, isothermal elastic constants, and bulk elastic moduli

Pressure (GPa)		Unit cell parameters			C_{11}	C_{22}	C_{33}	C_{12}	C_{13}	C_{23}	C_{44}	C_{55}	C_{66}	K	G
Calculated	Corrected	a (Å)	b (Å)	c (Å)	(GPa)	(GPa)	(GPa)	(GPa)	(GPa)	(GPa)	(GPa)	(GPa)	(GPa)	(GPa)	(GPa)
50	35	2.693	8.795	6.621	756	559	690	219	184	279	132	93	197	373	162
75	60	2.644	8.587	6.505	888	660	830	304	247	365	168	119	256	466	195
100	85	2.605	8.418	6.412	1,010	755	959	387	309	448	198	148	307	555	225
125	110	2.572	8.275	6.335	1,126	843	1,083	466	376	535	228	165	353	643	248
150	135	2.543	8.152	6.269	1,239	930	1,198	546	436	613	253	186	395	726	271
175	160	2.518	8.041	6.211	1,346	1,017	1,312	628	497	693	276	207	434	810	291

Errors on elastic moduli are less than 1%

t normalized to shear modulus (i.e. (t/G) * 100), the texture index (F_2), and IPF maximum for Runs 1–3. The texture index is the squared integral over the OD and provides a measure of texture sharpness (Bunge 1982). F_2 is equal to 1 for random distribution, and a value greater than 1 indicates a textured sample. The F_2 is in units of m.r.d.^{2} but is generally given without units.

Crystallite size

Crystallite size is largest in Run 1 where conversion temperature is highest (2,100 K), and smallest in Run 2 where conversion temperature is low (1,800 K). Crystallite size in Run 3 is slightly lower than in Run 1, consistent with the conversion temperature of 2,025 K. Crystallite size measured from X-ray diffraction is the size of coherently diffracting domains rather than actual grain size and represents an average over a distribution. Variation in crystallite size is also qualitatively clear from raw diffraction images (Fig. 3). A spottier pattern indicates larger crystallite size sample, while a smoother pattern indicates smaller crystallites. Run 1 (Fig. 3a) exhibits the spottiest pattern compared with those of Run 2 (Fig. 3b) and Run 3 (Fig. 3c). Run 2 (Fig. 3b) has the smoothest diffraction rings, indicating that the sample is quite fine grained. Run 3 (Fig. 3c) is spottier than Run 2 (Fig. 3b), but not as spotty as Run 1 (Fig. 3a). These qualitative observations are in good agreement with crystallite size obtained from the Rietveld refinement. In all three runs, crystallite size is largest immediately after conversion to pPv. Upon compression, crystallite size is reduced (Table 2), likely due to the formation of subgrains. None of the samples could be recovered for ex situ analysis.

Stress results

Figure 4 shows the axial stress component t versus pressure for Runs 1–3. Initially, stress increases with pressure in all

Table 2 Pressure, unit cell parameters, crystallite (domain) size, microstrains, axial stress component, axial stress component normalized to shear modulus, texture index (F_2), and inverse pole figure (IPF) maximum from Rietveld refinement for Run 2

Fig. 5		Pressure	Unit cell parameters			Crystallite size	Microstrain	t	$(t/G) * 100$	F_2	IPF max
		(GPa)	a (Å)	b (Å)	c (Å)	(Å)		(GPa)	(%)	m.r.d.^{2}	m.r.d.
Run 1	*a*	81.1	2.6086 (1)	8.4524 (4)	6.4344 (2)	570 (8)	0.00184 (2)	2.25 (2)	1.03	1.14	1.65
	b	96.7	2.5838 (2)	8.3734 (7)	6.3767 (5)	319 (4)	0.00305 (3)	12.56 (4)	5.32	1.09	2.07
	–	109.7	2.5666 (2)	8.3059 (7)	6.3346 (5)	291 (4)	0.00318 (3)	12.64 (4)	5.07	1.09	2.01
	*c**	109.2	2.5667 (2)	8.3090 (6)	6.3376 (4)	263 (3)	0.00355 (4)	13.65 (4)	5.49	1.15	2.65
Run 2	*d*	82.5	2.6067 (1)	8.4447 (5)	6.4277 (3)	301 (2)	0.00203 (1)	2.20 (3)	0.95	1.15	1.78
	–	110.2	2.5637 (2)	8.3120 (7)	6.3326 (5)	237 (2)	0.00330 (5)	15.31 (5)	4.96	1.23	1.81
	e	135.7	2.5335 (2)	8.1969 (6)	6.2586 (4)	138 (1)	0.00279 (4)	15.47 (5)	6.34	1.29	1.70
	f†	134.6	2.5346 (3)	8.2073 (9)	6.2573 (6)	125 (1)	0.00184 (7)	13.88 (7)	6.58	1.14	1.92
Run 3	*h*	75.8	2.6168 (3)	8.490 (1)	6.4527 (9)	490 (5)	0.0001 (3)	2.10 (9)	0.99	1.68	7.57
	–	108.5	2.5684 (2)	8.3106 (6)	6.3387 (5)	473 (4)	0.00088 (7)	12.39 (5)	5.00	1.64	7.23
	–	131.9	2.5396 (4)	8.203 (1)	6.272 (1)	401 (5)	0.00154 (4)	17.3 (1)	6.42	1.76	8.29
	i‡	127.0	2.5457 (5)	8.219 (2)	6.288 (1)	367 (7)	0.00144 (8)	17.9 (2)	6.75	2.34	8.66

Associated errors are given in parentheses. F_2 is the mean-squared integral over the orientation distribution and provides a measure of texture sharpness. Letter designations correspond to IPFs given in Fig. 5

† Cell was allowed to sit for 10 h

‡ Cell was allowed to sit for 1 h

* Cell was allowed to sit for 14 h

three runs. Highest stress values are obtained in Run 3 with $t = 17.9$ GPa at a pressure of 127 GPa (Table 2; Fig. 4). For Runs 1 and 2, two distinct behaviors are observed. In the initial stages of compression, stress increases rapidly with pressure. In this initial phase, stress increase is more efficient in Runs 1 and 2 than in Run 3. After this initial phase, stress "saturates" in Runs 1 and 2 (Fig. 4). For Run 1, stress reaches 12.56 GPa at a pressure of 96.7 GPa (Table 2; Fig. 4) and then remains relatively constant up to a pressure of 109.7 GPa (Table 2; Fig. 4). After allowing the cell to sit for 14 h, pressure decreases slightly to 109.2 GPa and stress increases to 13.65 GPa. In Run 2, similar stress "saturation" is observed (Fig. 4), but stress is higher than in Run 1 (Table 2; Fig. 4). At 110.2 GPa, stress is 15.31 GPa in Run 2 compared with 12.64 GPa at 109.7 GPa in Run 1 (Table 2; Fig. 4). With pressure increase to 135.7 GPa in Run 2, stress only increases to 15.47 GPa (Table 2). After allowing this cell to sit for 10 h, pressure decreases to 134.6 GPa and stress decreases to 13.88 GPa (Table 2). For Run 3, no stress "saturation" is observed. Stress increases monotonically with pressure throughout the experiment (Table 2; Fig. 4). At the maximum pressure in Run 3 (131.9 GPa), stress is 17.3 GPa, significantly higher than stresses in Runs 1 and 2 (Table 2; Fig. 4). When the cell was allowed to sit for 1 h, pressure decreased to 127.0 GPa. This rapid decrease in pressure is attributed to a small leak in the gas membrane used to drive the cell in Run 3. During this time, stress increases to 17.9 GPa (Table 2).

Texture results

IPFs for the three runs are shown in Fig. 5. After conversion from amorphized enstatite to pPv, in Run 1 a weak and diffuse maximum (1.65 m.r.d.) is observed at 100 in the IPF (Fig. 5a). Upon compression, this rapidly changes to a maximum at 001 (Table 2; Fig. 5b). This 001 texture becomes stronger with further compression and allowing the cell to sit (i.e. time lag under applied stress) (Table 2; Fig. 5c). In Run 2, a similar texture to Run 1 is observed just after conversion from amorphized enstatite (Fig. 5d). The texture strength in Run 2 is similar, with an IPF maximum of 1.78 m.r.d, versus 1.65 m.r.d. in Run 1 (Table 2). In contrast to Run 1, this texture changes little with further compression to 136 GPa (Fig. 5e). After allowing the cell to sit for 10 h, a weak maximum at 001 appears (Fig. 5f). Transformation textures are very different in Run 3 than in the first two runs. After transformation from the Pv phase, pPv exhibits a strong (7.57 m.r.d.) maximum at 001 (Fig. 5h). This texture remains stable with further compression (Fig. 5i). At the highest pressures in this run, texture strength has increased to 8.66 m.r.d. (Table 2; Fig. 5i).

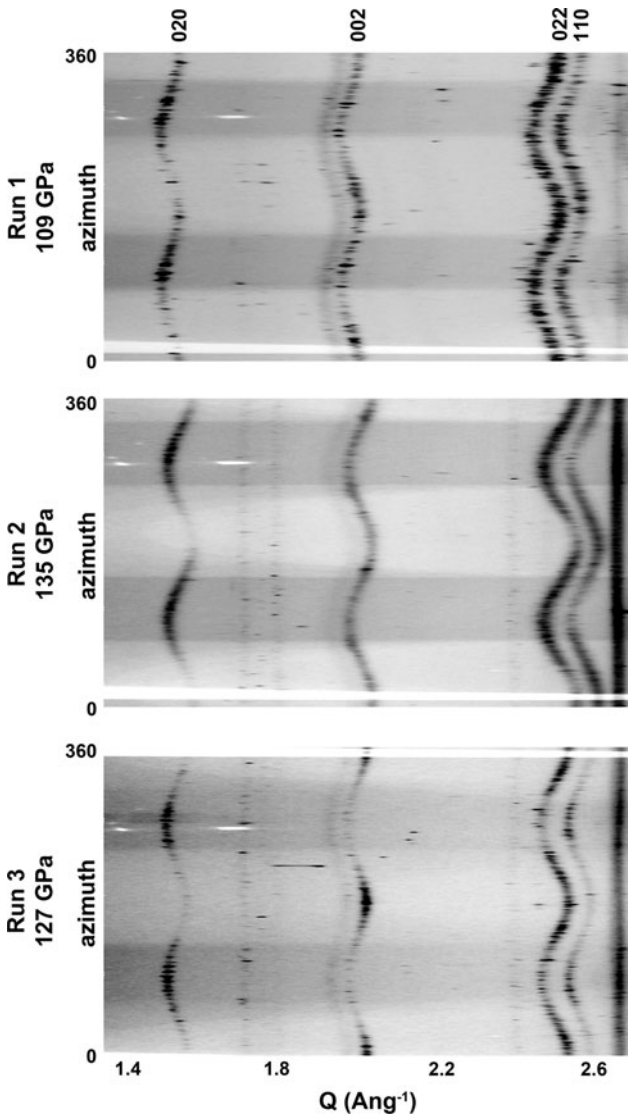

Fig. 3 Raw diffraction images from Runs 1–3. Relative grain size is qualitatively illustrated by the spottiness of the diffraction images. Run 1 is the spottiest of the three runs and has the coarsest crystallite size. Run 2 has the smoothest diffraction rings and has the smallest crystallite size, while Run 3 is intermediate to the other two runs. These qualitative observations are consistent with crystallite size obtained from Rietveld refinement (Table 2)

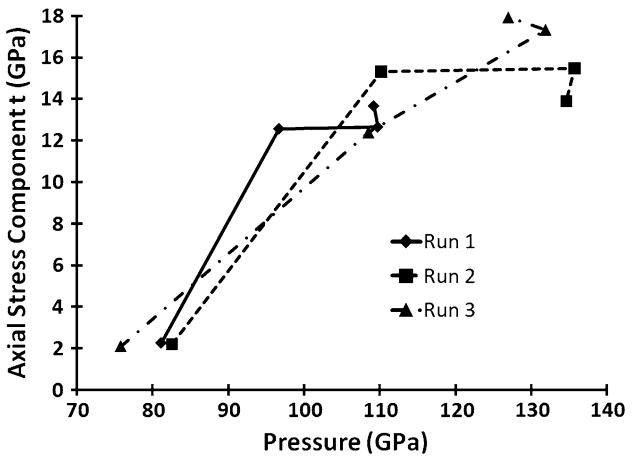

Fig. 4 Axial stress component t plotted versus pressure for Runs 1–3. Lines are guides for the eye only. Runs 1 and 2 exhibit similar behavior where stress initially increases with pressure but then saturates at higher compression. Run 1 that has the coarsest grain size exhibits stress saturation at lower values of *t* than Run 2 that is a finer-grained sample. Run 3 does not exhibit stress saturation but rather stress continues to increase with pressure. Texture in Run 3 is considerably different than in Runs 1 and 2

Discussion

Texture and stress development

In Runs 1 and 2, the initial 100 texture is consistent with textures previously obtained in $MgGeO_3$ pPv (Merkel et al. 2006) and $MgSiO_3$ pPv (Merkel et al. 2007) and appears related to the phase transformation. The 001 texture that develops upon compression is a result of deformation and was also observed in $MgSiO_3$ pPv (Miyagi et al. 2010). In Run 1, texture evolution is quite pronounced and occurs quickly upon compression (between 81.1 and 109.2 GPa) (Table 2; Fig. 5a–c). In Run 2, the 001 maximum is only observed at the end of the run after pressure was increased to 135.7 GPa and the cell was allowed to sit under stress for 10 h. This maximum is small and weak (Fig. 5f), indicating only minor deformation has occurred even though pressure and stress are higher than in Run 1. Note that stresses are lower in Run 1 than in Run 2 (peak stresses are 13.65 and 15.47 GPa, respectively) (Table 2).

Okada et al. (2010) hypothesized that in very high pressure studies (above 100 GPa), sample thickness may be too small for significant deformation to occur. But sample thickness does not explain the difference in Runs 1 and 2. The set-up of these two runs is nearly identical. The same DAC was used, anvils were of the same specifications (150/300 μm beveled anvils, 8° bevel angle), the same gasket type was used, gaskets were pre-compressed to the same (30 μm) thickness, and the same size sample chamber (50 μm diameter) was used. Conversion to pPv occurred at very similar pressures (Table 2). The only significant difference between these two runs is the laser heating temperature used for conversion and resulting difference in crystallite size which is for Run 1 approximately twice that of Run 2 (Table 2). It is known that fine-grained aggregates exhibit higher yield strength than coarse-grained aggregates (Hall–Petch effect) due to impedance of dislocations by grain boundaries. Thus, Run 2 (smaller crystallites) should have higher yield strength, and it should be harder to induce texture development than in Run 1 (larger crystallites).

Increased yield strength in fine-grained aggregates also is a likely explanation why Merkel et al. (2006, 2007) only

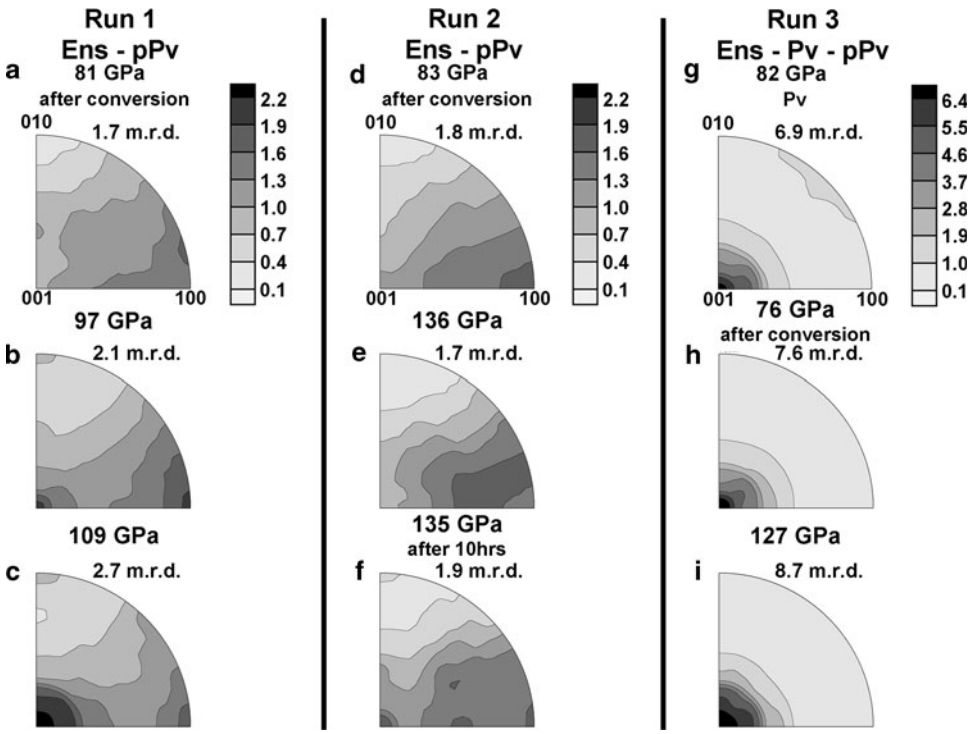

Fig. 5 IPFs of the compression direction for Runs 1–3. IPFs are equal-area upper-hemisphere projection and scale is in m.r.d. Conditions are given in Table 2. Run 1 is shown in **a**–**c**, Run 2 in **d**–**f,** and Run 3 in **g**–**i**. In Runs 1 and 2, conversion to pPv was directly from enstatite starting material, and textures immediately after exhibit a weak 100 texture (**a**, **d**). In Run 3, conversion to pPv was from the Pv phase, and prior to conversion to pPv, Pv exhibits a strong 001 texture (**g**). After transformation from Pv to pPv, a strong 001 transformation texture is obtained (**h**). Compression in Run 1 induces rapid texture evolution to a 001 texture (**c**), while in Run 2, this evolution is considerably weaker (**f**). In Run 3, the initial 001 texture component remains stable during compression (**i**)

observed 100 type textures. These studies converted to the pPv phase at relatively low temperatures of 1,600 K at 104 GPa in Merkel et al. (2006) and 1,700 K for 20 min, followed by 2,000 K for 15 min at 145 GPa in Merkel et al. (2007). Their diffraction images (Fig. 1 of Merkel et al. 2006 and Fig. 1 of Merkel et al. 2007) show smooth diffraction lines, indicating a fine-grained aggregate. Consequently, yield strength was likely high and differential stress too low (8.9 GPa at 124 GPa) to induce significant plastic deformation upon further compression. The present study obtained stresses of 13.65 GPa and 15.47 GPa for Runs 1 and 2, respectively. Run 3 exhibits different texture and stress evolution than Runs 1 and 2. After transformation from Pv, pPv has a strong maximum at 001 (Fig. 5h). This is consistent with Okada et al. (2010). In Runs 1 and 2, the initial texture after the conversion is due to transformation rather than deformation. Likewise, the initial 001 texture in pPv is likely due to the Pv to pPv transformation. This is well documented in $MgSiO_3$ Pv transformed from a variety of starting materials (Wenk et al. 2004, 2006; Miyagi 2010b). Upon deformation, this texture remains at 001, becoming slightly stronger (Fig. 5i), consistent with deformation textures in Runs 1 and 2.

Run 3 does not exhibit the same trend of stress saturation as observed in the first two runs. Stress in Run 3 continues to increase with pressure and final stresses are higher than in Runs 1 or 2 (Fig. 4; Table 2). This does not seem to be due to the crystallite size. Conversion temperature in this sample was slightly lower than in Run 1 (2,025 K). Crystallite size in Run 3 is slightly smaller than Run 1 but considerably larger that Run 2 (Table 2). Again, it is unlikely that sample volume is too small to induce plastic deformation as differential stress is very high in this sample. The high strength of this sample is likely related to the strong (7.57 m.r.d.) transformation texture (Fig. 5h).

Considering the transformation texture has a 001 maximum, similar to those generated by deformation, one must look to the plastic properties to understand stress evolution. Deformation of pPv has been extensively modeled by several authors (Merkel et al. 2006, 2007; Miyagi et al. 2008a) using the viscoplastic self-consistent code (VPSC) (Tomé and Canova 2000). Modeling by Miyagi et al. (2008a) showed that slip on {011} or (001) planes generates textures with (001) at high angles to compression; however, slip on {011} also produces a shoulder toward 010 (see Fig. 8 of Miyagi et al. 2008a). Only slip on the (001) plane produces a concentrated maximum at 001 (Merkel et al. 2006, 2007; Miyagi et al. 2008a). This is similar to textures after deformation in Run 1 and throughout Run 3. In Run 2, the maximum that develops at 001 is weak and thus hard to compare.

If slip on (001) is dominant in $MgGeO_3$ pPv, this explains the stress evolution of Run 3. The Schmidt factor determines whether a slip system is oriented favorably for deformation. The Schmidt factor is defined as $\cos\phi\cos\lambda$, where ϕ is the angle between the slip plane normal and the applied stress and λ is the angle between the slip direction and the applied stress. If the Schmidt factor is high, then

the slip system is favored to deform, and if it is zero, deformation cannot occur on the system. In Run 3, there is a strong transformation texture of (001) nearly perpendicular to compression (Fig. 5h). As the angle between the applied stress and (001) approaches 90°, the Schmidt factor goes to zero for (001) slip. For deformation to occur, a harder slip system must be activated and yield strength will be highest in this direction. In Run 3, crystals are predominantly oriented with (001) planes at high angles to a compression; thus, yield strength is higher than an aggregate with crystals in weaker orientations (e.g. Runs 1 and 2). This is why stress continues to increase monotonically in Run 3. The strong 001 texture results in a plastically hard aggregate, so bulk yielding largely does not occur.

The effect of slip direction on textures

Miyagi et al. (2008a) showed that for some cases, slip direction can be determined from compression textures. To address the effect of slip direction on texture development for slip on (001), we model Run 1, as this run exhibits the most pronounced texture evolution. For these simulations, we use VPSC version 6 with a tangent approximation for the inclusion–matrix interaction. A Voce hardening law was applied, and rate sensitivity with a stress exponent of 3 was assumed for all slip systems. The initial transformation texture in Run 1 (Fig. 5a) is used as a starting point for the simulation. Using 2000 grains, we apply an incremental deformation path to 20% compressive strain. Three models are run, favoring slip in the (001) plane but in different slip directions, [100], [010], and [011]. Table 3 shows critical resolved shear stresses (CRSS) and slip system activities for the three models shown. CRSS were chosen such that slip was most active in the (001) plane, and the most active slip system accommodated approximately 40–50% of deformation with the remainder evenly dispersed among the other slip systems. Compared with the experimental texture development in Run 1 (Fig. 4), slip on (001)[100] (Fig. 6a) provides the best match. In the experiment, deformation produces a maximum centered on 001 (Fig. 5c). Slip on (001)[010] and (001)[110] both produce maxima distinctly offset from 001 (Fig. 6b, c) while slip on (001)[100] produces a maximum centered on 001 (Fig. 6a). In the experiment, the initial maximum at 100 (Fig. 5a) does not become significantly stronger during deformation (Fig. 5c). For simulations of slip on (001)[010] and (001)[110], the maximum at 100 becomes significantly stronger during compression (Fig. 6b, c) and is nearly as strong as the maximum near 001. Only (001)[100] slip produces the strongest maximum centered at 001 with a weaker secondary maximum at 100 (Fig. 5a). This being said, it is possible that the activity of auxiliary slip systems could affect secondary features of the IPF and thus the determination of slip direction is more tentative. Unfortunately, the effect of slip direction textures for slip on the (001) plane is not as pronounced as it is for the (010) plane (Miyagi et al. 2008a).

Transformation textures

For Runs 1 and 2, conversion to pPv directly from pressure-amorphized enstatite resulted in a 001 transformation texture (Fig. 5a, d). One possible explanation for the generation of texture during a phase transformation is minimization of strain energy. For PPv, [010] is the elastically soft direction and for the minimization of elastic strain energy, [010] is expected to align with the compression direction. However, this is not what is observed. For silicate, Pv conversion from enstatite to Pv results in a strong 001 texture in the Pv phase (Wenk et al. 2004, 2006; Miyagi 2010b). This is likely due to a structural relationship between enstatite and silicate Pv, resulting in texture inheritance by the Pv phase (Miyagi 2010b). Texture inheritance is well established in high-pressure and high-temperature phases of iron (Merkel et al. 2004; Miyagi et al. 2008b). For silicate Pv, the transformation texture generated by the enstatite to perovskite transformation is quite strong (Wenk et al. 2004, 2006; Miyagi 2010b), while for enstatite to pPv, the texture in pPv is rather weak. In the experiments reported here, the enstatite phase became highly pressure amorphized prior to conversion to pPv. Unfortunately, the enstatite phase is too disordered to determine texture, but it is plausible that the transformation texture from a highly disordered enstatite would be relatively weak.

In Run 3, transformation from the Pv phase (initially synthesized in situ from enstatite) results in a strong 001 transformation texture in pPv, consistent with Okada et al. (2010). This transformation texture is, however, in contrast to transformation textures observed by Walte et al. (2009) in $CaIrO_3$ pPv, transformed from the Pv phase. After the transformation, a texture of (100) planes at high angles to the compression direction was observed in $CaIrO_3$ pPv. In that study, $CaIrO_3$ Pv did not appear to exhibit significant texture prior to transformation, and a transformation relationship between $CaIrO_3$ Pv and pPv was ruled out (Walte et al. 2009). This is also quite different from the present study where a significant (001) texture is observed in $MgGeO_3$ Pv (Fig. 5g).

The 001 texture observed in $MgGeO_3$ Pv (Fig. 5g) has also been obtained in silicate Pv, synthesized from enstatite (Wenk et al. 2004, 2006; Miyagi 2010b). This provides some support that the germanate Pv-pPv system should be a good analog for the silicate system. After conversion, $MgGeO_3$ pPv also has a strong maximum at 001 (Fig. 5h). The strong textures before and after conversion seem to

Table 3 CRSS and slip system activities (ACT) for the VPSC models are shown in Fig. 6

Fig. 6	(010)[100]		(010)<101>		{110}<−110>		(100)[010]		(001)[100]		(001)[010]		(001)<110>		{011}<100>		{011}<0−11>		{111}<101>	
	CRSS	ACT (%)	CRSS	ACT (%)	CRSS	ACT (%)	CRSS	ACT (%)	CRSS	ACT (%)	CRSS	ACT (%)	CRSS	ACT (%)	CRSS	ACT (%)	CRSS	ACT (%)	CRSS	ACT (%)
a	50	5	50	3	75	5	50	5	1	52	25	8	25	15	75	1	75	7	200	0
b	50	6	50	1	75	8	50	6	50	14	1	41	25	6	75	7	75	10	200	2
c	50	6	50	1	75	8	50	6	35	13	10	5	10	48	75	3	75	9	200	1

Letter designations *a*, *b*, and *c* refer to IPFs shown in Fig. 6. Activities given in the table are the average of the slip systems activity during deformation

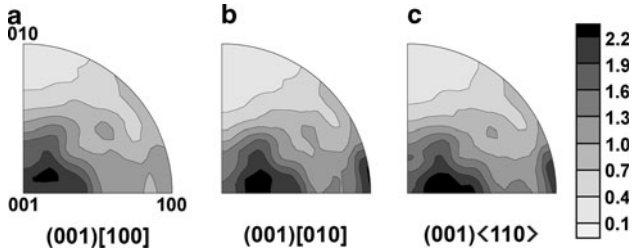

Fig. 6 VPSC results for dominant slip on (001)[100] (**a**), (001)[010] (**b**), and (001)⟨110⟩ (**c**). CRSS and slip system activities for these models are given in Table 3. The transformation texture of Fig. 5a was used as a starting texture for these models. Dominant slip (001)[100] provides the best match to the experimental data (Fig. 5c)

imply a structural relationship between the Pv and pPv phases and suggest that (001) Pv becomes (001) pPv. Previous theoretical work proposed that the phase transformation from Pv to pPv occurs by stretching of the Pv structure along [210], resulting in the following relationships between the two structures $\langle 1\bar{1}0\rangle_{Pv} \rightarrow [100]_{pPv}$, $[110]_{Pv} \rightarrow [010]_{pPv}$, and $[001]_{Pv} \rightarrow [001]_{pPv}$ (Tsuchiya et al. 2004). Thus, [001] is preserved between the two structures as is observed in our experiment. Alternatively, Oganov et al. (2005) predicted for the Pv to pPv transformation that a family of intermediate polytypes exist and the phase transformation occurs by sliding along the Pv (010)[100] system, which becomes $\{110\}\langle 1\bar{1}0\rangle$ in pPv. If the phase transformation is accomplished by sliding along these systems, this results in (001) Pv becoming (001) in pPv, also consistent with Run 3.

Slip systems in post-perovskites and analogs for $MgSiO_3$ post-perovskite

Here, we present robust evidence that at room temperatures and high pressures, $MgGeO_3$ pPv slips predominantly on (001) planes. Slip on (001) is most likely dominant in the [100] direction, but this is based on subtle features in the IPFs and is a more tentative conclusion than the slip plane. This is in contrast to (100) or {110} slip proposed by Merkel et al. (2006, 2007). Slip on (001)[100] has been predicted to be dominant for $MgGeO_3$ pPv using first-principles modeling of dislocation cores with the Peierls–Nabarro model (Metsue et al. 2009), consistent with our experimental data.

Recent experimental results for $MgSiO_3$ pPv documented texture development during deformation that was consistent with dominant slip on (001) at room temperature and high pressure (Miyagi et al. 2010). The fact that $MgGeO_3$ and $MgSiO_3$ exhibit the same transformation textures for the enstatite to Pv transformation and for the enstatite to pPv transformation, as well as exhibiting consistent deformation textures, suggests that the $MgGeO_3$

system is indeed a good analog for $MgSiO_3$. Since $MnGeO_3$ pPv appears to also exhibit (001) slip during deformation (Hirose et al. 2010), it may also be a good analog for $MgSiO_3$ pPv. Indeed germanates have long been considered to be good analogs for silicates based on crystal chemistry and slip systems (Navrotsky and Ross 1988; Dupas-Bruzek et al. 1998).

By contrast, $CaIrO_3$ pPv slips predominantly on (010)[100] at a wide range of conditions and exhibits no change in slip systems with temperature, pressure or strain rate (Miyajima et al. 2006; Yamazaki et al. 2006; Walte et al. 2007, 2009; Niwa et al. 2007; Miyagi et al. 2008a; Miyajima and Walte 2009). Thus, $CaIrO_3$ appears to be a poor analog for the deformation behavior of $MgSiO_3$ pPv in the lower mantle. There are several other pPv-structured compounds that have not been investigated for texture development, among them is $NaMgF_3$ pPv (Liu et al. 2005; Martin et al. 2006a, b; Hustoft et al. 2008b).

Implications for D″ anisotropy

There are significant limitations to these experiments that make extrapolation of these results to the D″ challenging. Experiments were performed at low temperature and high stress. These conditions are clearly far different from those in the deep earth, where material deforms at high temperature as well as high pressure but low stress and over geologic timescales (see also Wenk et al. 2011, Appendix B). In our experiments, we explore the most active slip system during dislocations glide at room temperature and high pressure/stress conditions. At high temperatures and low stress conditions, deformation can also be accommodated through diffusion processes. Within a crystal dislocation, climb can occur and serves to reduce work hardening. Climb is accomplished by diffusion of vacancies (Nabarro 1948). Grain boundary diffusion may occur and is also due to diffusion of vacancies (Coble 1963). During diffusion, creep deformation is accomplished via grain boundary sliding. Neither climb nor diffusion creep directly contribute to preferred orientation, and activation of these processes at high temperatures is unlikely to significantly affect preferred orientation, other than strengthening or weakening texture developed by dislocation glide.

A more significant concern is that at higher temperatures CRSS curves may cross and the most active slip system may change. Some minerals such as olivine have CRSS that are dependent on temperature, pressure, stress, and water content (e.g. Karato et al. 2008). For $MgSiO_3$ pPv, this is poorly constrained, and high-pressure and high-temperature deformation studies need to be performed in the future to establish whether deformation mechanisms change with temperature. Such high-temperature deformation experiments at extreme pressure are very challenging. However, progress has been made, both using the resistive-heated (Liermann et al. 2009) and in situ laser-heated (Miyagi et al. 2008b) DAC, in conjunction with radial diffraction.

Of the pPv-structured compounds, $CaIrO_3$ pPv has been studied experimentally over a wide range of pressure, temperature, and stress conditions and does not exhibit a change in the dominant (010) slip system (Miyajima et al. 2006; Yamazaki et al. 2006; Walte et al. 2007; Miyagi et al. 2008a; Miyajima and Walte 2009). Similarly, the $MnGeO_3$ pPv analog exhibits dominant 001 slip up to 2,000 K (Hirose et al. 2010). This is consistent with this study and the most recent room temperature deformation experiments on $MgSiO_3$ pPv (Miyagi et al. 2010). Based on observations of these pPv-structured compounds, it is plausible that slip in pPv structures is not very temperature sensitive.

If (001) slip is dominant in $MgSiO_3$ pPv at D″ conditions, this has considerable geodynamic significance. Simulations of texture development during convection, assuming the previously inferred (100) and (110) slip, produce patterns of anisotropy with $V_{SH} < V_{SV}$ in contrast seismic observations (Merkel et al. 2007). However, when (001) slip is used to model anisotropy development in D″, anisotropy of $V_{SH} > V_{SV}$ as well as an anti-correlation between P- and S-waves is predicted, consistent with seismic observations (Miyagi et al. 2010; Wenk et al. 2011). A recent seismic study of the D″ region using differential S and ScS splitting also found that anisotropy beneath subduction zones is best matched if (001) slip in pPv is assumed (Nowacki et al. 2010). Thus, a range of evidence from seismology, geodynamics, and mineral physics experiments seems to be converging on (001) slip as the dominant slip system for pPv in the D″.

Conclusions

The new DAC experiments establish that the starting material has a significant effect on transformation textures in $MgGeO_3$ pPv, with a weak 100 texture developing during the enstatite to pPv transformation and a strong 001 texture developing during the Pv to pPv transformation. In the transformed $MgGeO_3$ pPv, slip occurs primarily on (001) planes and tentatively in the [100] direction. Crystallite size, which can be controlled by laser heating temperatures, has an important effect on yield strength (Hall–Petch effect). The high yield strength of fine-grained samples makes it difficult to induce plastic flow with the limited strain attainable in the DAC. Transformation textures also have an influence on active slip systems. A strong 001 transformation texture results in a plastically hard aggregate with only minor texture change since 001

slip is unfavorable in compression. In this study, it has become possible to separate transformation and deformation textures and thus better define deformation mechanisms in high-pressure pPv structures. The derived dominant (001) slip, when combined with geodynamic models, predicts S-wave anisotropy and an anti-correlation between P- and S-waves that are consistent with seismic observations.

Acknowledgments This work was performed at HPCAT (Sector 16), Advanced Photon Source (APS), Argonne National Laboratory. HPCAT is supported by CIW, CDAC, UNLV, and LLNL through funding from DOE-NNSA, DOE-BES, and NSF. APS is supported by DOE-BES, under Contract No. DE-AC02-06CH11357. We would like to thank T. S. Duffy at Princeton University for kindly providing the starting material. L.M. acknowledges support of the Bateman Fellowship at Yale University. S.S. acknowledges support from NSF, CDAC, and UC Berkeley's laboratory fee grant. H.R.W acknowledges support from CDAC and NSF Grant No. EAR0836402 and EAR0757608. We appreciate the help of Y. Meng at HPCAT.

References

Ammann MW, Brodholt JP, Wookey J, Dobson DP (2010) First-principles constraints on diffusion in lower-mantle minerals and a weak D″ layer. Nature 465:462–465

Blöchl PE (1994) Projector augmented-wave method. Phys Rev B 50:7953–17979

Bunge H-J (1982) Texture analysis in materials science—mathematical methods. Butterworths, London

Carrez P, Ferré D, Cordier P (2007a) Peierls-Nabarro model for dislocations in MgSiO3 post-perovskite calculated at 120 GPa from first principles. Philos Mag 87:3229–3247

Carrez P, Ferre D, Cordier P (2007b) Implications for plastic flow in the deep mantle from modelling dislocations in $MgSiO_3$ minerals. Nature 446:68–70

Coble RL (1963) A model for boundary diffusion controlled creep in polycrystalline materials. J Appl Phys 34:1679–1682

Dupas-Bruzek C, Tingle TN, Green HW II, Doukhan N, Doukhan J (1998) The rheology of olivine and spinel magnesium germanate (Mg_2GeO_4): TEM study of the defect microstructures. Phys Chem Miner 25:501–514

Garnero EJ, McNamara AK (2008) Structure and dynamics of Earth's lower mantle. Science 320:626–628

Hammersley AP (1997) FIT2D: an introduction and overview. ESRF Internal Report, ESRF97HA02T

Helmberger D, Lay T, Ni S, Gurnis M (2005) Deep mantle structure and the postperovskite phase transition. Proc Natl Acad Sci USA 102:17257–17263

Hirose K, Nagaya Y, Merkel S, Ohishi Y (2010) Deformation of $MnGeO_3$ post-perovskite at lower mantle pressure and temperature. Geophys Res Lett 37:L20302

Hohenberg P, Kohn W (1964) Inhomogeneous electron gas. Phys Rev 136:B864–B871

Hunt SA, Weidner DJ, Li L, Wang L, Walte NP, Brodholt JP, Dobson DP (2009) Weakening of calcium iridate during its transformation from perovskite to post-perovskite. Nat Geosci 2:794–797

Hustoft J, Shim S, Kubo A, Nishiyama N (2008a) Raman spectroscopy of $CaIrO_3$ postperovskite up to 30 GPa. Am Miner 93:1654–1658

Hustoft J, Catalli K, Shim S, Kubo A, Prakapenka VB, Kunz M (2008b) Equation of state of $NaMgF_3$ postperovskite: implication for the seismic velocity changes in the D″ region. Geophys Res Lett 35:L10309

Iitaka T, Hirose K, Kawamura K, Murakami M (2004) The elasticity of the $MgSiO_3$ post-perovskite phase in the Earth's lowermost mantle. Nature 430:442–445

Ischia G, Wenk H-R, Lutterotti L, Berberich F (2005) Quantitative Rietveld texture analysis of zirconium from single synchrotron diffraction images. J Appl Crystallogr 38:377–380

Karato SI, Jung H, Katayama I, Skemer P (2008) Geodynamic significance of seismic anisotropy of the upper mantle: new insights from laboratory studies. Annu Rev Earth Planet Sci 36:59–95

Karki BB (2000) Thermal pressure in MgO and $MgSiO_3$ perovskite at lower mantle conditions. Am Miner 85:1447–1451

Karki BB, Stixrude L, Wentzcovitch RM (2001) High-pressure elastic properties of major materials of Earth's mantle from first principles. Rev Geophys 39:507–534

Kohn W, Sham LJ (1965) Self-consistent equations including exchange and correlation effects. Phys Rev 140:A1133–A1138

Kresse G, Furthmüller J (1996a) Efficient iterative schemes for ab initio total-energy calculations using a plane-wave basis set. Phys Rev B 54:11169–11186

Kresse G, Furthmüller J (1996b) Efficiency of ab initio total energy calculations for metals and semiconductors using a plane-wave basis set. Comput Mater Sci 6:15–50

Kresse G, Joubert D (1999) From ultrasoft pseudopotentials to the projector augmented-wave method. Phys Rev B 56:1758–1775

Kubo A, Kiefer B, Shen G, Prakapenka VB, Cava RJ, Duffy TS (2006) Stability and equation of state of the post-perovskite phase in $MgGeO_3$ to 2 Mbar. Geophys Res Lett 33:L12S12

Kubo A, Kiefer B, Shim S, Shen G, Prakapenka VB, Duffy TS (2008) Rietveld structure refinement of $MgGeO_3$ post-perovskite phase to 1 Mbar. Am Miner 93:965–976

Lay T, Garnero EJ (2007) Reconciling the post-perovskite phase with seismological observations of lowermost mantle structure. In: Hirose K et al (ed) Post-perovskite: the last mantle phase transition, AGU monograph, vol 174. pp 129–154

Liermann HP, Merkel S, Miyagi L, Wenk HR, Shen G, Cynn H, Evans WJ (2009) Experimental method for in situ determination of material textures at simultaneous high pressure and high temperature by means of radial diffraction in the diamond anvil cell. Rev Sci Instrum 80:104501

Liu H, Chen J, Hu J, Martin CD, Weidner DJ, Häusermann D, Mao HK (2005) Octahedral tilting evolution and phase transition in orthorhombic $NaMgF_3$ perovskite under pressure. Geophys Res Lett 32:L04304

Loubet N, Ribe NM, Gamblin Y (2009) Deformation modes of subducted lithosphere at the core-mantle boundary: an experimental investigation. Geochem Geophys Geosyst 10:Q10004

Lutterotti L (2006) http://www.ing.unitn.it/~maud/Tutorial/sizestrain/InstrumentalBroadening.pdf

Lutterotti L, Matthies S, Wenk HR, Schultz AS, Richardson JW (1997) Combined texture and structure analysis of deformed limestone from time-of-flight neutron diffraction spectra. J Appl Phys 81:594

Martin CD, Crichton WA, Liu H, Prakapenka V, Chen J, Parise JB (2006a) Rietveld structure refinement of perovskite and post-perovskite phases of $NaMgF_3$ (Neighborite) at high pressures. Am Miner 91:1703–1706

Martin CD, Crichton WA, Liu H, Prakapenka V, Chen J, Parise JB (2006b) Phase transitions and compressibility of $NaMgF_3$ (Neighborite) in perovskite- and post-perovskite-related structures. Geophys Res Lett 33:L11305

Matthies S, Humbert M (1993) The realization of the concept of a geometric mean for calculating physical constants of polycrystalline materials. Physica Status Solidi (b) 177:K47–K50

Matthies S, Vinel GW (1982) On the reproduction of the orientation distribution function of texturized samples from reduced pole figures using the conception of a conditional ghost correction. Physica Status Solidi (b) 112:K111–K114

Matthies S, Priesmeyer HG, Daymond MR (2001) On the diffractive determination of single-crystal elastic constants using polycrystalline samples. J Appl Crystallogr 34:585–601

McNamara AK, van Keken PE, Karato SI (2002) Development of anisotropic structure in the Earth's lower mantle by solid-state convection. Nature 416:310–314

McNamara AK, Keken PE, Karato SI (2003) Development of finite strain in the convecting lower mantle and its implications for seismic anisotropy. J Geophys Res 108:2230

Merkel S, Wenk HR, Gillet P, Mao HK, Hemley RJ (2004) Deformation of polycrystalline iron up to 30 GPa and 1000 K. Phys Earth Planet Interiors 145:239–251

Merkel S, Kubo A, Miyagi L, Speziale S, Duffy TS, Mao HK, Wenk HR (2006) Plastic deformation of $MgGeO_3$ post-perovskite at lower mantle pressures. Science 311:644–646

Merkel S, McNamara AK, Kubo A, Speziale S, Miyagi L, Meng Y, Duffy TS, Wenk HR (2007) Deformation of (Mg, Fe)SiO3 post-perovskite and D″ anisotropy. Science 316:1729–1732

Metsue A, Carrez P, Mainprice D, Cordier P (2009) Numerical modelling of dislocations and deformation mechanisms in $CaIrO_3$ and $MgGeO_3$ post-perovskites—comparison with $MgSiO_3$ post-perovskite. Phys Earth Planet Interiors 174: 165–173

Miyagi L (2010b) Deformation and texture development in deep earth mineral phases: implications for seismic anisotropy and dynamics. Ph.D. thesis, University of California Berkeley

Miyagi L, Nishiyama N, Wang Y, Kubo A, West DV, Cava RJ, Duffy TS, Wenk HR (2008a) Deformation and texture development in $CaIrO_3$ post-perovskite phase up to 6 GPa and 1300 K. Earth Planet Sci Lett 268:515–525

Miyagi L, Kunz M, Knight J, Nasiatka J, Voltolini M, Wenk HR (2008b) In situ phase transformation and deformation of iron at high pressure and temperature. J Appl Phys 104:103510–103519

Miyagi L, Kanitpanyacharoen W, Kaercher P, Lee KKM, Wenk HR (2010) Slip systems in $MgSiO_3$ post-perovskite: implications for D″ anisotropy. Science 329:1639–1641

Miyajima N, Walte N (2009) Burgers vector determination in deformed perovskite and post-perovskite of $CaIrO_3$ using thickness fringes in weak-beam dark-field images. Ultramicroscopy 109:683–692

Miyajima N, Ohgushi K, Ichihara M, Yagi T (2006) Crystal morphology and dislocation microstructures of $CaIrO_3$: a TEM study of an analogue of the $MgSiO_3$ post-perovskite phase. Geophys Res Lett 33:L12302

Monkhorst HJ, Pack JD (1976) Special points for Brillouin-zone integration. Phys Rev B 13:5188–5192

Murakami M, Hirose K, Kawamura K, Sata N, Ohishi Y (2004) Post-perovskite phase transition in $MgSiO_3$. Science 304:855–858

Nabarro FRN (1948) Deformation of crystals by the motion of single ions. In: Report of a conference on strength of solids, vol 75. The physical Society, London, pp 75–90

Navrotsky A, Ross N (1988) Study of the $MgGeO_3$ polymorphs (ortho-pyroxene, clinopyroxene, and ilmenite structures) by calorimetry, spectroscopy and phase-equilibria. Am Miner 73:1355–1365

Niwa K, Yagi T, Ohgushi K, Merkel S, Miyajima N, Kikegawa T (2007) Lattice preferred orientation in $CaIrO_3$ perovskite and post-perovskite formed by plastic deformation under pressure. Phys Chem Mineral 34:679–686

Nowacki A, Wookey J, Kendall J (2010) Deformation of the lowermost mantle from seismic anisotropy. Nature 467: 1091–1094

Oganov AR, Ono S (2004) Theoretical and experimental evidence for a post-perovskite phase of $MgSiO_3$ in Earth's D″ layer. Nature 430:445–448

Oganov AR, Brodholt JP, Price G (2001) Ab initio elasticity and thermal equation of state of $MgSiO_3$ perovskite. Earth Planet Sci Lett 184:555–560

Oganov AR, Martonak R, Laio A, Raiteri P, Parrinello M (2005) Anisotropy of Earth's D" layer and stacking faults in the $MgSiO_3$ post-perovskite phase. Nature 438:1142–1144

Okada T, Yagi T, Niwa K, Kikegawa T (2010) Lattice-preferred orientations in post-perovskite-type $MgGeO_3$ formed by transformations from different pre-phases. Phys Earth Planet Interiors 180:195–202

Panning M, Romanowicz B (2004) Inferences on flow at the base of Earth's mantle based on seismic anisotropy. Science 303: 351–353

Panning M, Romanowicz B (2006) A three-dimensional radially anisotropic model of shear velocity in the whole mantle. Geophys J Int 167:361–379

Perdew JP, Burke K, Ernzerhof M (1996) Generalized gradient approximation made simple. Phys Rev Lett 77:3865–3868

Popa NC, Balzar D (2002) An analytical approximation for a size-broadened profile given by the lognormal and gamma distributions. J Appl Crystallogr 35:338–346

Santillán J, Shim S, Shen G, Prakapenka VB (2006) High-pressure phase transition in Mn_2O_3: application for the crystal structure and preferred orientation of the $CaIrO_3$ type. Geophys Res Lett 33:L15307

Shim S (2008) The post-perovskite transition. Annu Rev Earth Planet Sci 36:569–599

Shim S, Duffy TS, Jeanloz R, Shen G (2004) Stability and crystal structure of $MgSiO_3$ perovskite to the core-mantle boundary. Geophys Res Lett 31:L10603

Singh AK (1993) The lattice strains in a specimen (cubic system) compressed nonhydrostatically in an opposed anvil device. J Appl Phys 73:4278–4286

Singh AK, Balasingh C, Mao HK, Hemley RJ, Shu J (1998) Analysis of lattice strains measured under nonhydrostatic pressure. J Appl Phys 83:7567–7575

Speziale S, Lonardelli I, Miyagi L, Pehl J, Tommaseo CE, Wenk HR (2006) Deformation experiments in the diamond-anvil cell: texture in copper to 30 GPa. J Phys Condens Matter 18:S1007–S1020

Stackhouse S, Brodholt JP (2007) The high-temperature elasticity of MgSiO3 post-perovskite. In: Hirose K et al (ed) Post-perovskite: the last mantle phase transition, AGU monograph, vol 174. pp 99–113

Stackhouse S, Brodholt JP, Wookey J, Kendall J, Price GD (2005) The effect of temperature on the seismic anisotropy of the perovskite and post-perovskite polymorphs of $MgSiO_3$. Earth Planet Sci Lett 230:1–10

Tomé CN, Canova G (2000) Self-consistent modeling of heterogeneous plasticity. In: Kocks UF et al (ed) Texture and anisotropy: preferred orientations in polycrystals and their effect on material properties. Cambridge University Press, Cambridge, pp 466–510

Tsuchiya T, Tsuchiya J (2007) Structure and elasticity of Cmcm $CaIrO_3$ and their pressure dependences: Ab initio calculations. Phys Rev B 76:144119

Tsuchiya T, Tsuchiya J, Umemoto K, Wentzcovitch RM (2004) Phase transition in $MgSiO_3$ perovskite in the Earth's lower mantle. Earth Planet Sci Lett 224:241–248

Usui Y, Tsuchiya J, Tsuchiya T (2010) Elastic, vibrational, and thermodynamic properties of $MgGeO_3$ postperovskite investigated by first principles simulation. J Geophys Res 115:B03201

Walte NP, Heidelbach F, Miyajima N, Frost D (2007) Texture development and TEM analysis of deformed $CaIrO_3$: implications

for the D″ layer at the core-mantle boundary. Geophys Res Lett 34:L08306

Walte NP, Heidelbach F, Miyajima N, Frost DJ, Rubie DC, Dobson DP (2009) Transformation textures in post-perovskite: understanding mantle flow in the D″ layer of the earth. Geophys Res Lett 36:L04302

Wenk HR, Lonardelli I, Pehl J, Devine JM, Prakapenka VB, Shen G, Mao HK (2004) In situ observation of texture development in olivine, ringwoodite, magnesiowustite and silicate perovskite at high pressure. Earth Planet Sci Lett 226:507–519

Wenk HR, Lonardelli I, Merkel S, Miyagi L, Pehl J, Speziale S, Tommaseo CE (2006) Deformation textures produced in diamond anvil experiments, analysed in radial diffraction geometry. J Phys Condens Matter 18:S933–S947

Wenk HR, Cottaar S, Tomé CN, McNamara AK, Romanowicz B (2011) Deformation in the lowermost mantle: from polycrystal plasticity to seismic anisotropy. Earth Planet Sci Lett 306:33–45

Wentzcovitch RM, Tsuchiya T, Tsuchiya J (2006) $MgSiO_3$ post-perovskite at D″ conditions. Proc Natl Acad Sci USA 103:543–546

Wookey J, Kendall J (2007) Seismic anisotropy of post-perovskite and the lowermost mantle. In: Hirose K et al (eds) Post-perovskite: the last mantle phase transition, AGU monograph, vol 174. pp 171–189

Yamazaki D, Yoshino T, Ohfuji H, Ando J, Yoneda A (2006) Origin of seismic anisotropy in the D'' layer inferred from shear deformation experiments on post-perovskite phase. Earth Planet Sci Lett 252:372–378